AGU PUBLICATIONS

JGR

Journal of Geophysical Research: Space Physics

RESEARCH ARTICLE
10.1002/2017JA024484

Key Points:
- Proton energy spectra are measured by the Van Allen Probes for two magnetic storms
- The most intense proton spectra are compared with theoretical limiting spectra
- Observations of the most intense proton spectra are consistent with self-limiting by EMIC wave scattering

Correspondence to:
D. Summers,
dsummers@mun.ca

Citation:
Summers, D., Shi, R., Engebretson, M. J., Oksavik, K., Manweiler, J. W., & Mitchell, D. G. (2017). Energetic proton spectra measured by the Van Allen Probes. *Journal of Geophysical Research: Space Physics*, *122*, 10,129–10,144. https://doi.org/10.1002/2017JA024484

Received 16 JUN 2017
Accepted 18 SEP 2017
Accepted article online 26 SEP 2017
Corrected 30 OCT 2017
Published online 17 OCT 2017

This article was corrected on 30 OCT 2017. See the end of the full text for details.

Energetic Proton Spectra Measured by the Van Allen Probes

Danny Summers[1], Run Shi[1,2,3], Mark J. Engebretson[4], Kjellmar Oksavik[5,6,7], Jerry W. Manweiler[8], and Donald G. Mitchell[9]

[1]Department of Mathematics and Statistics, Memorial University of Newfoundland, St. John's, Newfoundland, Canada, [2]Department of Space Physics, School of Electronic Information, Wuhan University, Wuhan, China, [3]Center for Space Physics, Boston University, Boston, MA, USA, [4]Department of Physics, Augsburg College, Minneapolis, MN, USA, [5]Birkeland Centre for Space Science, Department of Physics and Technology, University of Bergen, Bergen, Norway, [6]The University Centre in Svalbard, Longyearbyen, Norway, [7]Center for Space Science and Engineering Research, Virginia Tech, Blacksburg, VA, USA, [8]Fundamental Technologies LLC, Lawrence, KS, USA, [9]Space Department, The Johns Hopkins University Applied Physics Laboratory, Laurel, MD, USA

Abstract We test the hypothesis that pitch angle scattering by electromagnetic ion cyclotron (EMIC) waves can limit ring current proton fluxes. For two chosen magnetic storms, during 17–20 March 2013 and 17–20 March 2015, we measure proton energy spectra in the region $3 \leq L \leq 6$ using the RBSPICE-B instrument on the Van Allen Probes. The most intense proton spectra are observed to occur during the recovery periods of the respective storms. Using proton precipitation data from the POES (NOAA and MetOp) spacecraft, we deduce that EMIC wave action was prevalent at the times and *L*-shell locations of the most intense proton spectra. We calculate limiting ring current proton energy spectra from recently developed theory. Comparisons between the observed proton energy spectra and the theoretical limiting spectra show reasonable agreement. We conclude that the measurements of the most intense proton spectra are consistent with self-limiting by EMIC wave scattering.

1. Introduction

Ion pitch angle scattering by electromagnetic ion cyclotron (EMIC) waves is considered to be a significant ring current loss mechanism (e.g., Kennel & Petschek, 1966; Cornwall et al., 1970; Lundblad & Soraas, 1978; Søraas et al., 1999; Erlandson & Ukhorskiy, 2001; Yahnina et al., 2002; Summers, 2005; Fraser et al., 2006; Jordanova et al., 2007; Yahnin & Yahnina, 2007; Engebretson et al., 2008; Sakaguchi et al., 2008; Usanova et al., 2010; Spasojevic et al., 2011; Xiao et al., 2012; Søraas et al., 2013; Yuan et al., 2014, 2016; Xiong et al., 2016). In this paper, we revisit the concept of the limitation of ring current ion flux by EMIC waves. Kennel and Petschek (1966) originally suggested that, under certain conditions, electromagnetic wave gain due to convective growth along a magnetic field line would equal the wave energy lost due to wave reflection at the (ionospheric) ends of the field line and that this balance would produce a self-limiting particle flux. This idea was proposed to apply to both EMIC wave-ion interactions and whistler mode wave-electron interactions. Schulz and Davidson (1988) were able to obtain the Kennel-Petschek limiting particle spectrum ($J \propto 1/E$) at large energy *E* in a nonrelativistic regime. Summers et al. (2009), in a relativistic study, replaced the aforementioned wave energy criterion used by Kennel and Petschek (1966) by a condition that specifies the wave gain over a given convective length scale and obtained expressions for the limiting differential and integral electron fluxes at a given *L*-shell. Mauk and Fox (2010) obtained Kennel-Petschek-type differential flux limits by using flexible analytic fits to measured electron distributions and applied their results to solar system electron radiation belts. Nonlinear wave gain effects were included in the limiting electron flux problem by Summers et al. (2011). Tang and Summers (2012) compared measured average electron differential and integral fluxes at Saturn with corresponding Kennel-Petschek limits over a range of *L*-shells ($4.5 < L < 11$). Mauk (2013, 2014) obtained limiting ion spectra moderated by EMIC waves in a cold multi-ion background plasma and compared them with measured planetary ring current spectra.

Summers and Shi (2014) were able, for the first time, to solve the limiting electron flux problem in a relativistic regime without assuming a predetermined form for the particle distribution. They showed that the limiting electron differential flux moderated by whistler mode waves is determined by an integral equation that can be solved by standard numerical techniques. Subsequently, Summers and Shi (2015) likewise showed in a

relativistic regime that the limiting ion differential flux subject to scattering by EMIC waves in a cold multi-ion background plasma is also given by an integral equation that must be solved numerically.

In the present study, we test the validity of the formulation of the limiting ion flux by Summers and Shi (2015) by comparing numerical (theoretical) solutions for the limiting flux with experimental proton flux profiles. Specifically, we measure proton differential flux profiles in the region $3 \leq L \leq 6$ over two chosen magnetic storms using data from the RBSPICE-B instrument on the Van Allen Probes. In section 2 we describe the data analysis associated with RBSPICE-B, and in section 3 we present the proton flux observations obtained. In section 4 we provide a condensed theoretical account of how we determine the limiting proton energy spectrum. Typically, regions of EMIC wave activity are highly localized and hence relatively difficult to observe by the Van Allen Probes. Therefore, as a useful proxy for EMIC wave activity, we use proton precipitation events observed by the POES (NOAA and MetOp) spacecraft. Various studies collectively provide firm evidence of the link between EMIC wave activity and proton precipitation spikes, and we briefly review these studies in section 5. We describe our observations of POES precipitation events in section 6. In section 7 we show comparisons of the observed proton spectra with the theoretical limiting solutions. Finally, in section 8 we provide a brief summary and state our conclusions.

2. Data Analysis

RBSPICE is a time-of-flight versus total energy instrument on board the Van Allen Probes (spacecraft A and B) with a perigee of ~600 km and an apogee of ~5.8 R_E (Mauk et al., 2012). The orbital period of the Van Allen Probes is approximately 9 h. RBSPICE measures ions over the energy range from ~20 keV to ~1 MeV, as well as electrons in the range from 25 keV to 1 MeV. The instrument further distinguishes the ion composition. It provides high-resolution measurements of energy and pitch angle for hydrogen (10–600 keV), helium (75–600 keV), and oxygen (40 keV–1 MeV) (Mitchell et al., 2013). In the present investigation, we focus on hydrogen. The proton abundances are from the time-of-flight versus total energy instrument feature (Mitchell et al., 2013) and cover the energy range ~10 keV to ~600 keV. The total energy of a particle that transits the detector system is measured by a solid state detector. Ion velocities are determined by measuring the time-of-flight of a particle through the instrument between collisions using an entrance and exit foil. We utilize the level 3-PAP data that are already pitch angle binned. For the two magnetic storm periods (specified below) that we have chosen to study, RBSPICE-B was operational with its high voltage system fully engaged, covering a wider range of L-shells than RBSPICE-A. Therefore, the data from RBSPICE-B are used for this study. The data can be found via the website http://rbspiceb.ftecs.com/Level_3PAP/. To obtain the proton differential flux profile as a function of energy at different L-shells, the measured proton differential flux at 90° pitch angle is selected and binned using 0.1 R_E bins. The McIlwain L-shell parameter is computed for 90° particles using the OP77Q external field (Olson & Pfitzer, 1982) and IGRF internal field (Finlay et al., 2010).

3. RBSPICE-B Observations

The geomagnetic storm periods considered in this study are as follows:

Case 1: **17–20 March 2013**

and

Case 2: **17–20 March 2015**

As illustrated in Figure 1, Case 1 comprises Van Allen Probe B orbits 527–535, while Case 2 comprises orbits 2,469–2,477. For L-shells of interest in the present work, namely, $3 \leq L \leq 6$, Van Allen Probe B is located basically on the nightside for both Cases 1 and 2. Time profiles of the *Dst* and *Kp* indices for Cases 1 and 2 are respectively given in the bottom two panels of Figures 3 and 6.

Case 1 involves a strong storm with minimum $Dst = -132$ nT. The main phase extends from 06:00 UT, 17 March to 21:00 UT, 17 March, and the recovery phase throughout 18–20 March 2013 is considered. Substorm activity, as indicated by *Kp* levels, is strong during the main phase and weak during the recovery phase.

Case 2 comprises a severe storm with minimum $Dst = -223$ nT. The main phase occurs during 07:30 UT, 17 March to 22:45 UT, 17 March, and the recovery phase during 18–20 March 2015 is considered. Substorm activity is extreme during the main phase and remains strong throughout the recovery phase.

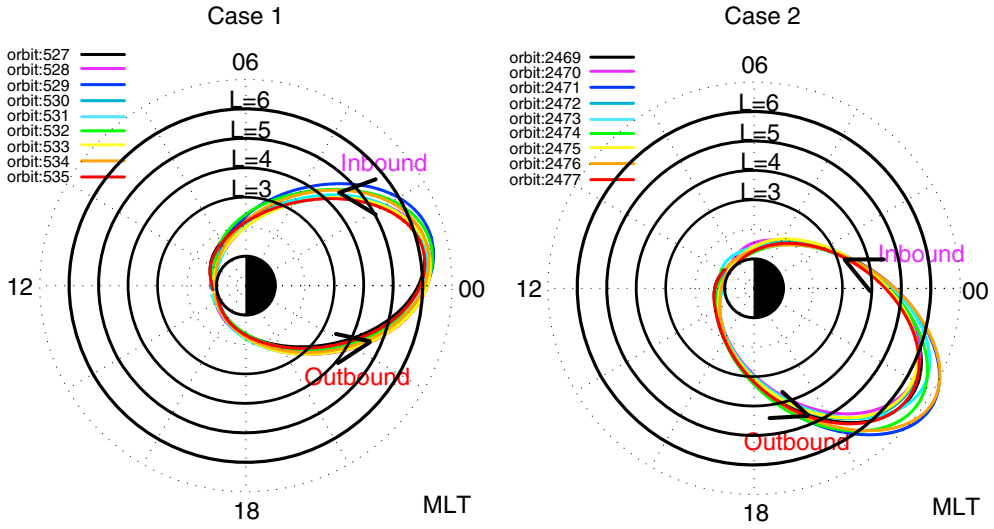

Figure 1. Trajectories of Van Allen Probe B projected onto the equator for Cases 1 and 2, labeled by color-coded orbit number.

In describing Cases 1 and 2 as respectively "strong" and "severe" storms, we have used the classification of magnetic storms by Loewe and Prölss (1997). We should note here in fact that the physical concept that we are addressing in this paper, namely, self-limiting of trapped particle fluxes by wave scattering, is not necessarily associated only with storms. For instance, this concept is also valid during moderate substorm activity in the absence of magnetic storms.

Figure 2 provides a broad overview of the variation of proton differential flux intensity at energies $E = 55$ keV, 100 keV, and 600 keV, with respect to L-shell, over the duration of the magnetic storm periods Cases 1 and 2. For Case 1, at $E = 55$ keV, 100 keV, following initiation of the storm, there is a broad increase in flux over the L-shell range $4 \lesssim L \lesssim 5$, which is maintained throughout the recovery phase; at $E = 600$ keV, there is a relatively

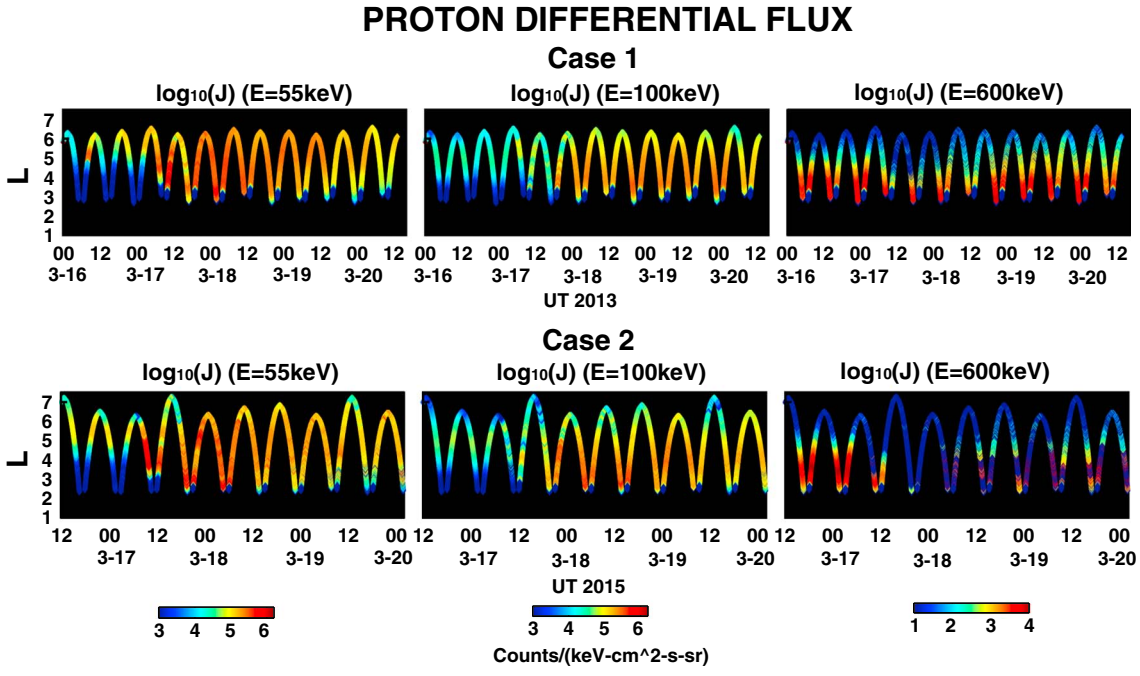

Figure 2. Local proton differential flux measured by RBSPICE-B as a function of McIlwain L-shell and universal time UT, for Cases 1 and 2, at each of the energies $E = 55$ keV, 100 keV, and 600 keV.

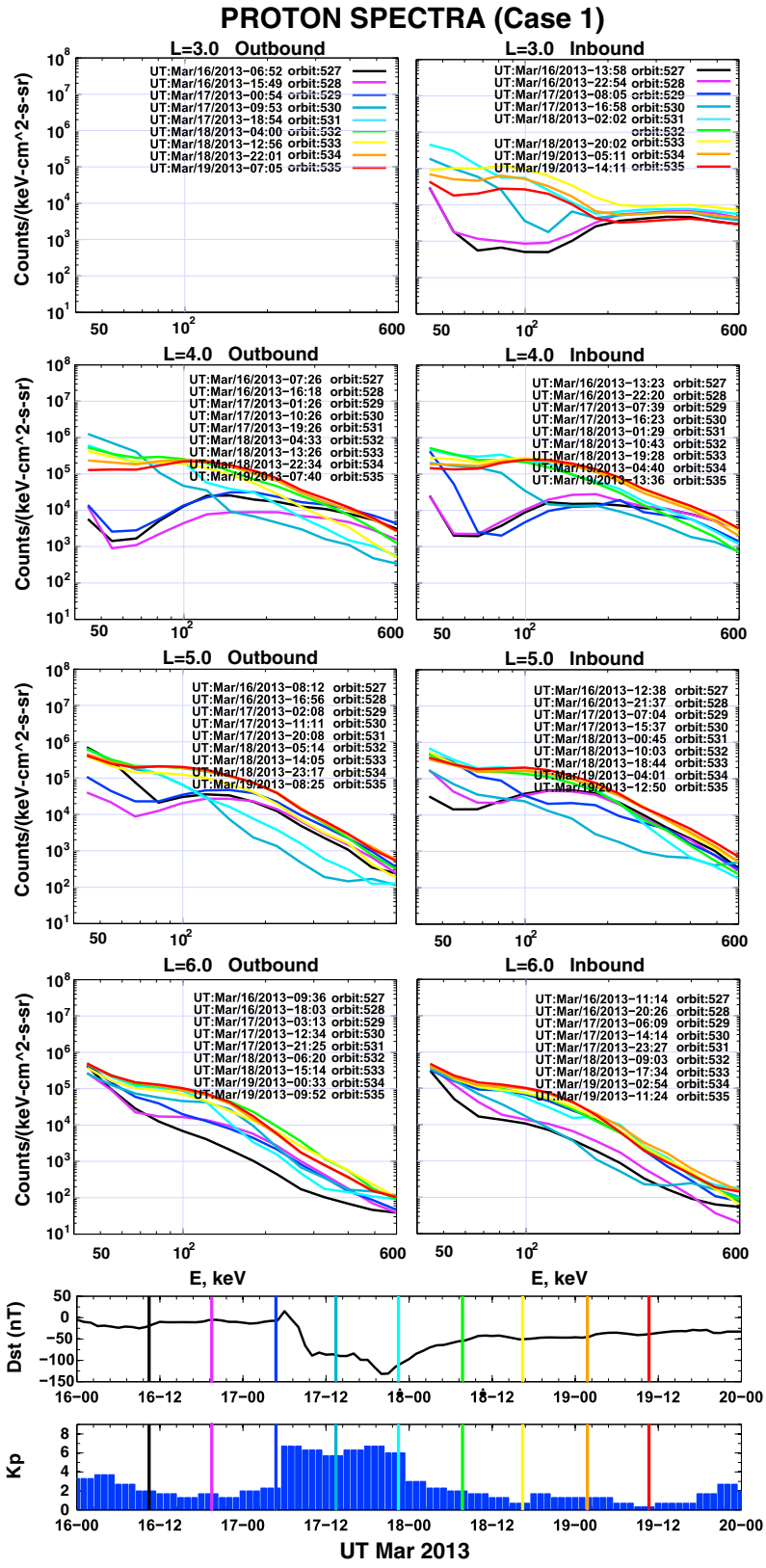

Figure 3. Proton spectra measured by RBSPICE-B for Case 1. The spectra are color-coded by orbit number at the indicated *L*-shells. In the bottom panels are time profiles of the *Dst* and *Kp* indices. The vertical colored lines indicate the times at apogee for each color-coded orbit.

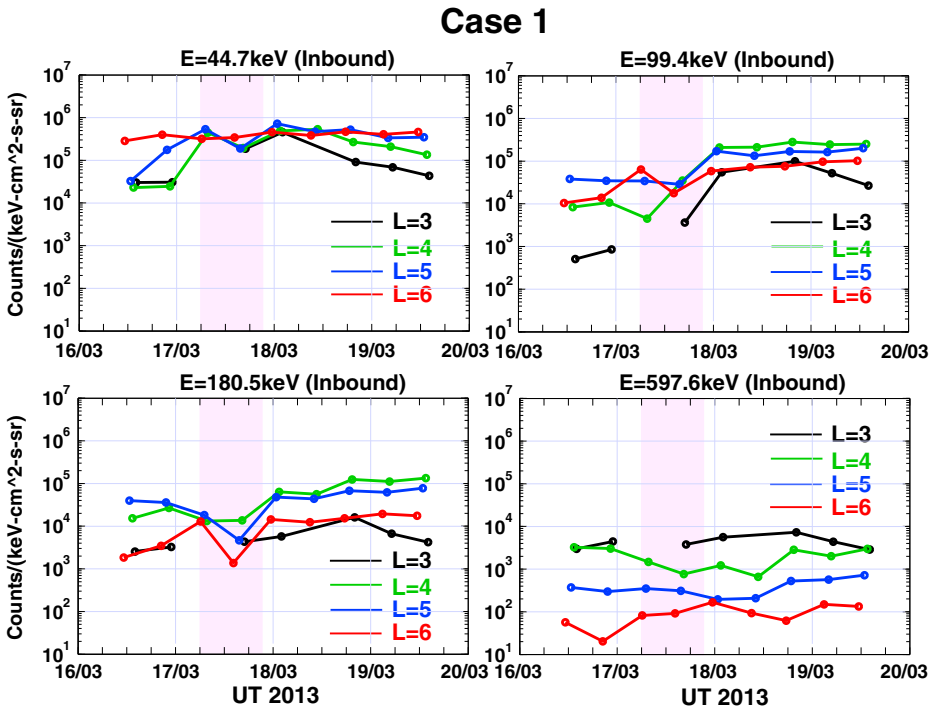

Figure 4. Proton fluxes from RBSPICE-B (inbound passes) as a function of universal time UT for Case 1 at the given energies and *L*-shells. The shaded region represents the storm main phase.

insignificant increase in flux as a result of the storm, and the flux remains at a low level over all *L*-shells during the storm. For Case 2, at $E = 55$ keV, 100 keV, there is a broad increase in flux over *L*-shells, $3 \lesssim L \lesssim 4$, due to the storm; at $E = 600$ keV, dependent on *L*-shell, fluxes undergo a net loss or insignificant increase as a result of the storm.

In the upper eight panels of Figure 3 we show proton (differential) spectra for Case 1 at $L = 3$, 4, 5, and 6 for outbound and inbound satellite passes, with the spectra color-coded according to orbit number and universal time. In the lower panels showing the time profiles of the *Dst* and *Kp* indices, the vertical colored lines indicate times of apogee of RBSP-B. In general, a broad increase in spectral intensity is apparent over the course of the storm over most *L*-shells and energies. In particular, we observe the strong relatively flat spectrum over energies 50 keV–200 keV, at $4 \lesssim L \lesssim 5$, that is produced over the recovery period. We also observe that at each *L*-shell for which both outbound and inbound spectra are shown in Figure 3, the outbound and inbound spectra show very similar behavior. No proton data are available at $L = 3$ for the outbound passes in Case 1.

Figure 4 shows detailed time variations of proton fluxes for Case 1 over the course of the storm, for inbound passes, at each energy $E = 44.7$ keV, 99.4 keV, 180.5 keV, and 597.6 keV, for the *L*-shells $L = 3$, 4, 5, and 6. The colored rectangular region in each panel represents the duration of the main phase of the storm. The strong flux at $E = 44.7$ keV is maintained or increased at each *L*-shell during the storm. We note, in particular, the significant increases in flux, by about an order of magnitude over prestorm values, for energies $E = 99.4$ keV and $E = 180.5$ keV at $L = 4$. At $E = 597.6$ keV the relatively low prestorm flux does not significantly increase at any *L*-shell over the course of the storm. Figure 5 shows detailed time profiles of proton fluxes for Case 1 at the same energies and *L*-shells as Figure 4, but for outbound passes. Overall, Figures 4 and 5 indicate very similar behavior of the proton flux variations over the storm as measured during the inbound and outbound satellite passes.

Figure 6 shows proton spectra for Case 2 in an identical format to that used in Figure 3 for Case 1. Many features of the proton spectra shown in Figures 3 and 6 are similar, including the general intensification of the spectra during the course of the storm. However, the proton spectra in Figure 6, the case of a severe storm, differ from the spectra in Figure 3 in two significant ways. First, strong enhancements in spectra not only occur for $L = 4$ and 5 but also occur at $L = 3$. Second, the range of energies over which the enhanced

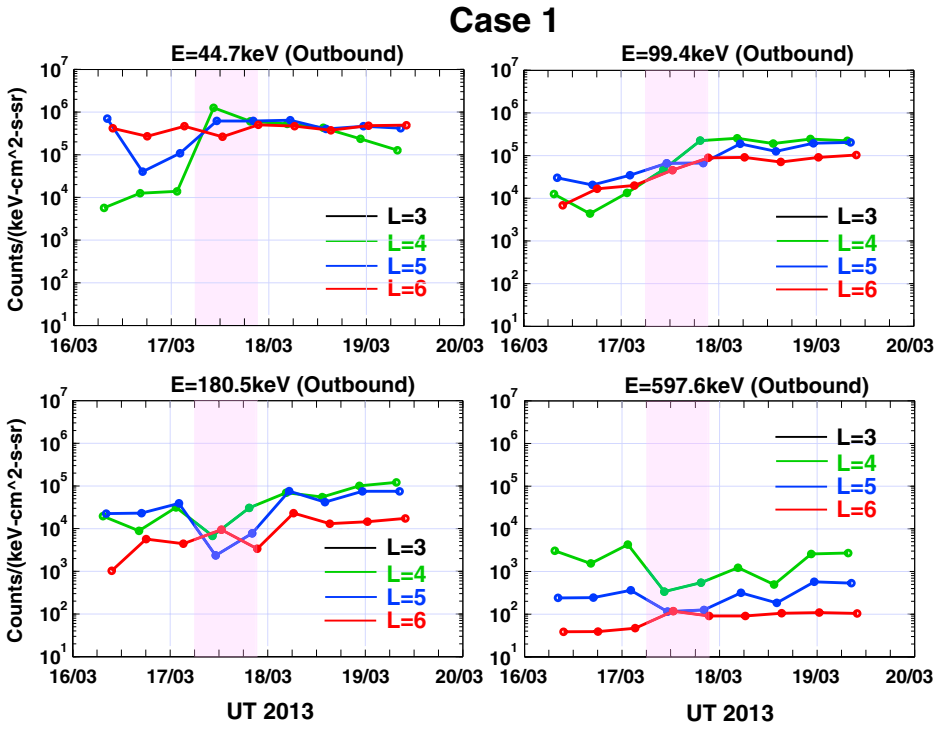

Figure 5. As in Figure 4, except for outbound passes.

spectra are largely "flat" is from 50 keV to approximately 300 keV. Time profiles of the proton fluxes for Case 2 at each of the energies E = 44.7 keV, 99.4 keV, 180.5 keV, and 597.6 keV for each L-shell, L = 3, 4, 5, and 6 are shown in Figure 7 for inbound passes and Figure 8 for outbound passes. We note, in particular, that at L = 3, the increase in flux for E = 99.4 keV is by 2 orders of magnitude, and for E = 180.5 keV, the increase in flux is well in excess of 1 order of magnitude over prestorm values. Even for this severe storm, at E = 597.6 keV, proton fluxes do not increase significantly at any L-shell.

4. Calculation of the Limiting Energy Spectrum

We consider field-aligned EMIC waves generated near the Earth's magnetic equator by a trapped energetic ring current proton population with an anisotropic distribution f given by

$$f(p_\parallel, p_\perp) = (\sin\alpha)^{2s} g(p), \tag{1}$$

where s (>0) is the pitch angle index and the function g describes the energy spectrum; $p = \sqrt{p_\parallel^2 + p_\perp^2}$, where $p_\parallel = \gamma v_\parallel/c$ and $p_\perp = \gamma v_\perp/c$ are the normalized parallel and perpendicular components of particle momentum; $v_\parallel$ and $v_\perp$ are the particle velocity components parallel and perpendicular to the background magnetic field, $v = \sqrt{v_\parallel^2 + v_\perp^2}$ is the particle speed, c is the speed of light, and $\gamma = \sqrt{1+p^2}$ is the Lorentz factor; $\alpha = \tan^{-1}(p_\perp/p_\parallel)$ is the particle pitch angle. The omnidirectional differential proton flux is then

$$J_{4\pi}(E) = 4\pi (m_p c)^2 \int_0^1 p^2 f \, d(\cos\alpha) = 2\pi^{3/2} \frac{\Gamma(s+1)}{\Gamma(s+3/2)} (m_p c)^2 p^2 g(p), \tag{2}$$

where Γ is the gamma function and m_p is the proton rest mass. The proton kinetic energy E is given by

$$E = \left(\sqrt{1+p^2} - 1\right) m_p c^2 \tag{3}$$

so that $p^2 = \left(\frac{E}{m_p c^2}\right)\left[\left(\frac{E}{m_p c^2}\right) + 2\right]$.

We suppose that the EMIC waves generated by the distribution (1) undergo a specified gain G in amplitude during propagation over a convective path length LR_E along a magnetic field line, where L denotes magnetic

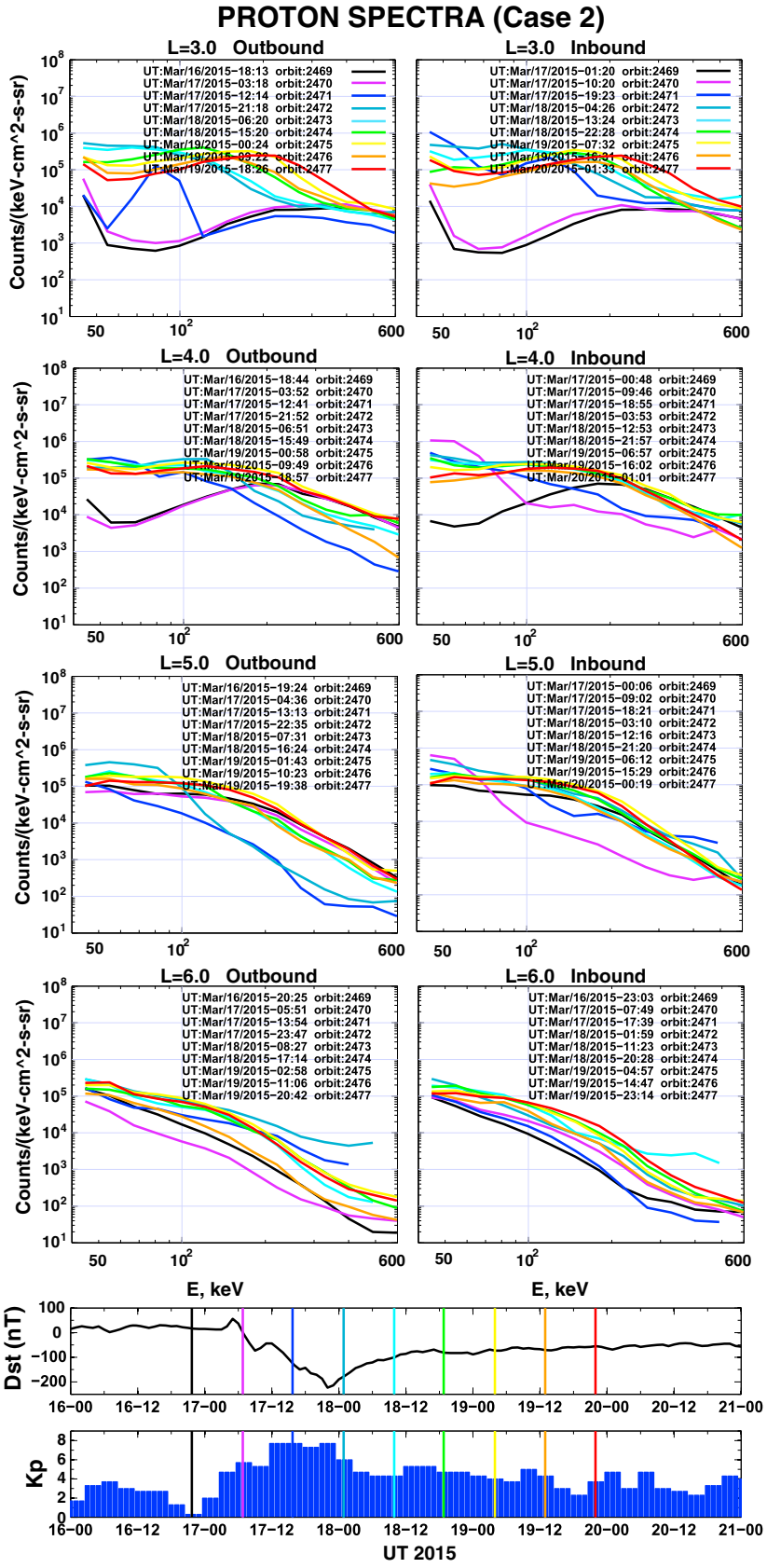

Figure 6. As in Figure 3, except for Case 2.

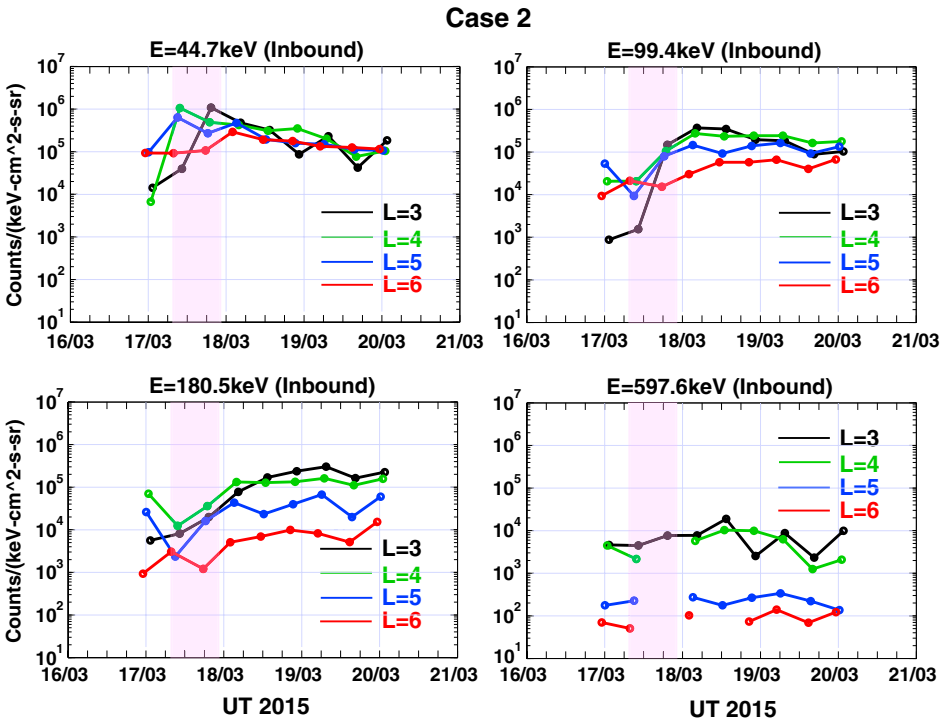

Figure 7. Proton fluxes from RBSPICE-B (inbound passes) as a function of universal time UT for Case 2 at the given energies and *L*-shells. The shaded region represents the storm main phase.

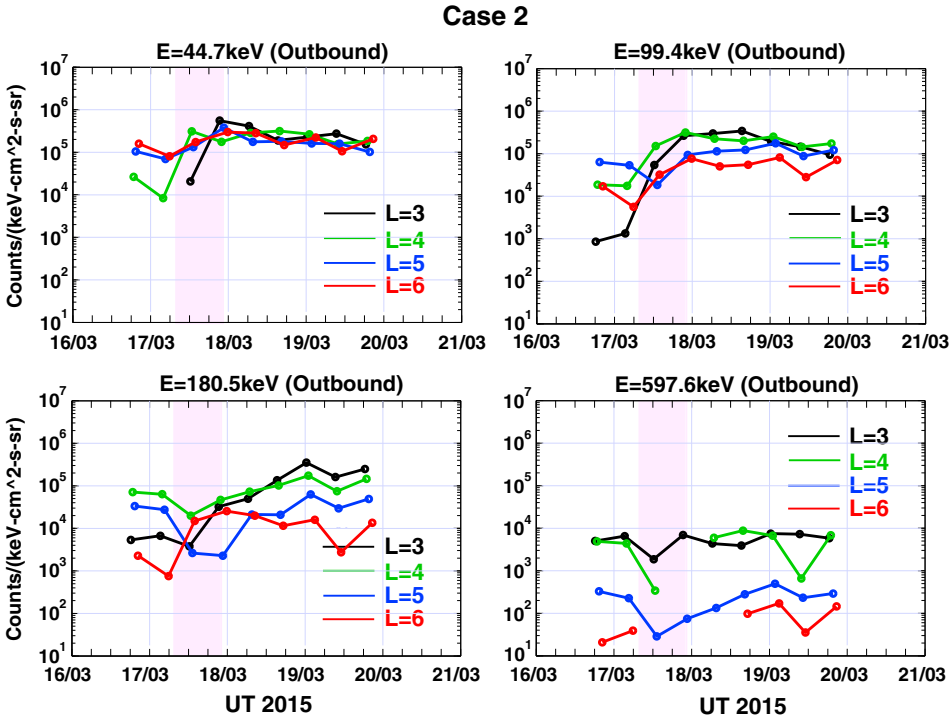

Figure 8. As in Figure 7, except for outbound passes.

shell and R_E is the Earth's radius. Then, as detailed by Summers and Shi (2015), it can be shown that a limiting energy distribution $g(p) = g^*(p)$ can be achieved where g^* is determined by the equation,

$$\int_{X_0}^{\infty}\left[1-\left(\frac{1-\gamma\omega/\Omega_p}{1-\gamma_0\omega/\Omega_p}\right)^2\frac{X_0}{X}\right]^s \cdot\left[\frac{s}{\gamma}-(1+s)\frac{\omega}{\Omega_p}-\frac{(1+s)}{\gamma}\left(\frac{\omega}{\Omega_p}\right)^2\frac{(1-\gamma\omega/\Omega_p)}{(1-\gamma_0\omega/\Omega_p)^2}X_0\right]g^*(p)dX, \quad (4)$$
$$= \frac{1}{(m_pc)^2}\cdot\frac{1}{2\pi^3}\cdot\frac{G}{m_pc^2}\cdot\frac{cB_E}{eR_E}\cdot\frac{(1-\gamma_0\omega/\Omega_p)^2}{L^4X_0}$$

where ω is the (real) wave frequency, $X = p^2$, $\gamma = \sqrt{1+X}$, and $\Omega_p = eB_0/(m_pc)$ is the proton gyrofrequency where e is the electronic charge. We assume that the background magnetic field strength B_0 equals the equatorial dipole value, $B_0 = B_E/L^3$. In addition, in equation (4), we have set $X_0 = p_0^2$ and $\gamma_0 = \sqrt{1+X_0}$, where p_0 is the minimum proton momentum for gyroresonance given by

$$p_0 = \left[n(\Omega_p/\omega) - \left[(\Omega_p/\omega)^2 + n^2 - 1\right]^{1/2}\right]/(n^2-1), \quad (5)$$

where $n = ck/\omega$ is the refractive index and k is the (real) wave number.

We further assume that the background plasma component is cold and contains hydrogen (H^+), helium (He^+), and oxygen (O^+) ions. The cold plasma dispersion relation for L-mode EMIC waves can be expressed as

$$n^2 = 1 - \frac{1}{a\varepsilon(\omega/\Omega_p)}\left\{\frac{1}{1+\varepsilon\omega/\Omega_p}+\frac{\eta_1}{\omega/\Omega_p-1}+\frac{\eta_2}{4\omega/\Omega_p-1}+\frac{\eta_3}{16\omega/\Omega_p-1}\right\}, \quad (6)$$

where $a = |\Omega_e|^2/\omega_{pe}^2$ is a cold plasma parameter, $|\Omega_e| = eB_0/(m_ec)$ is the electron gyrofrequency, and m_e is the electron rest mass; $\omega_{pe} = (4\pi N_0e^2/m_e)^{1/2}$ is the electron plasma frequency, and N_0 is the background electron number density; $\varepsilon = m_e/m_p$; $\eta_1 = N_1/N_0$, $\eta_2 = N_2/N_0$, and $\eta_3 = N_3/N_0$, where N_1, N_2, and N_3 are respectively the hydrogen, helium, and oxygen ion number densities. For charge neutrality we require that $\eta_1 + \eta_2 + \eta_3 = 1$.

Equation (4), which is an integral equation for g^*, is valid for all frequencies ω over which wave growth occurs. The equation can be readily transformed into a linear Volterra integral equation of the first kind (see Summers & Shi, 2015) and can be solved by standard numerical techniques, as given, for instance, by Press et al. (2007). Once the solution for g^* has been found, the limiting omnidirectional differential proton flux (from (2)) is then given by

$$J_{4\pi}^*(E) = 2\pi^{3/2}\frac{\Gamma(s+1)}{\Gamma(s+3/2)}(m_pc)^2X\,g^*(p), \quad (7)$$

where $E = \left(\sqrt{1+X}-1\right)m_pc^2$.

While analytical solutions of equation (4) are not readily found, Summers and Shi (2015) were able to obtain a useful asymptotic solution for g^* valid for large X (or, equivalently, large E) of the form $g^* \sim 1/X^{3/2}$ as $X \to \infty$. The corresponding asymptotic solution for the limiting energy spectrum $J_{4\pi}^*$ given by result (7) is found to be

$$J_{4\pi}^*(E) = \frac{cB_E}{\pi^{3/2}eR_E}\left(\frac{s+1}{s}\right)\frac{\Gamma(s+1)}{\Gamma(s+3/2)}\frac{G}{L^4E}, E\to\infty \quad (8)$$

The simple asymptotic solution (8) can be readily compared with observed particle spectra at large energy E. Further, solution (8) serves as a useful reference against which numerical solutions of equation (4) can be compared.

5. Relation of POES Observations of Proton Spikes to EMIC Wave Activity: A Brief Review

Literature over several decades has established a strong link between EMIC wave activity and particle precipitation spikes at midlatitudes. In particular, papers by Lundblad and Soraas (1978), Søraas et al. (1980, 1999),

Table 1
Times and Locations of NOAA/MetOp Observations of Precipitating Protons for Case 1 (2013)

Month/d	Time (UT)	MLT	Peak *L*	Min *L*	Max *L*	Amplitude	Spacecraft
3/18	00:29:00–00:30:00	15.00	3.81	3.79	3.82	6,000	NOAA15
3/18	01:17:00–01:19:00	15.90	3.97	3.93	4.01	2,000	NOAA19
3/18	13:12:00–13:13:00	12.90	3.93	3.87	3.98	30,000	NOAA19
3/18	18:11:00–18:12:00	10.00	4.26	4.12	4.39	200,000	MetOp2
3/19	03:34:00–03:38:00	6.60	4.28	4.19	4.36	90,000	NOAA16
3/19	07:03:00–07:05:00	6.00	4.38	4.33	4.42	8,000	NOAA16
3/19	17:05:00–17:06:00	9.80	3.93	3.85	4.00	60,000	MetOp1
3/20	05:37:00–05:38:00	7.20	3.93	3.90	3.96	10,000	MetOp2
3/20	07:20:00–07:21:00	3.20	3.70	3.64	3.76	10,000	NOAA15
3/20	09:39:00–09:41:00	10.40	3.82	3.78	3.86	8,000	NOAA16

Yahnina et al. (2000, 2003), and Sandanger et al. (2007) all use POES (Polar Operational Environmental Satellites) data (or earlier satellite data with similar instrumentation) to relate midlatitude proton spikes to EMIC wave activity. In the following paragraph we briefly discuss these papers and related studies, in order to place into context our own use (described in section 6) of POES proton precipitation events as evidence of EMIC wave activity.

The anisotropic pitch angle distribution of ring current protons provides free energy for EMIC waves, which leads to pitch angle diffusion, proton precipitation into the atmosphere, and the formation of stable auroral red (SAR) arcs at midlatitudes (Cornwall et al., 1971). Observations of energy spectra and pitch angle distributions have verified that the proton fluxes and pitch angle anisotropies in the ring current are sufficient to cause significant wave growth (Joselyn & Lyons, 1976). The pitch angle scattered ring current protons will precipitate into the midlatitude atmosphere, where low-altitude observations have identified proton precipitation spikes in connection with SAR arcs (Lundblad & Soraas, 1978). Søraas et al. (1980) related magnetic field pulsations on the ground (IPDP, intervals of pulsations with diminishing periods) to satellite observations of energetic protons equatorward of the isotropic proton precipitation. Søraas et al. (1999) linked the same midlatitude proton precipitation spikes to EMIC wave-particle interaction. Jordanova et al. (1996) modeled ring current proton precipitation due to EMIC wave scattering and found the maximum precipitation within regions of maximum EMIC wave activity. Yahnina et al. (2000, 2003) related the midlatitude proton precipitation spikes to EMIC wave activity via Pc1 and IPDP pulsations. Sandanger et al. (2007) also found observational evidence that EMIC wave activity can lead to additional scattering loss of relativistic electrons during geomagnetic storms.

Table 2
Times and Locations of NOAA/MetOp Observations of Precipitating Protons for Case 2 (2015)

Month/d	Time (UT)	MLT	Peak *L*	Min *L*	Max *L*	Amplitude	Spacecraft
3/18	22:55:30–22:56:30	18.60	3.13	3.10	3.15	2,000	NOAA15
3/18	23:30:00–23:30:45	21.40	3.16	3.12	3.20	7,000	MetOp2
3/18	23:30:45–23:31:00	21.30	3.05	3.00	3.10	5,000	MetOp2
3/19	00:23:30–00:24:30	21.60	2.95	2.92	2.97	2,000	MetOp1
3/19	05:25:00–05:26:00	3.20	3.10	3.08	3.12	4,000	NOAA15
3/19	05:54:30–05:56:30	7.80	3.04	3.00	3.10	10,000	MetOp2
3/19	05:54:30–05:56:30	7.70	3.18	3.16	3.25	10,000	MetOp2
3/19	07:38:00–07:39:00	7.50	3.20	3.10	3.30	50,000	MetOp2
3/19	07:38:30–07:39:30	6.40	3.25	3.03	3.47	20,000	NOAA18
3/19	10:29:30–10:30:30	10.90	3.33	3.28	3.37	100,000	MetOp2
3/20	04:16:00–04:17:00	10.30	3.29	3.24	3.33	40,000	MetOp1
3/20	04:25:30–04:26:30	3.50	3.17	3.04	3.30	1,000	NOAA19
3/20	14:37:00–14:38:00	2.20	3.15	3.14	3.16	1,000	NOAA19
3/20	15:07:30–15:08:00	16.30	3.12	3.08	3.15	10,000	NOAA18
3/20	19:42:30–19:43:30	3.00	3.07	3.04	3.09	2,000	NOAA19

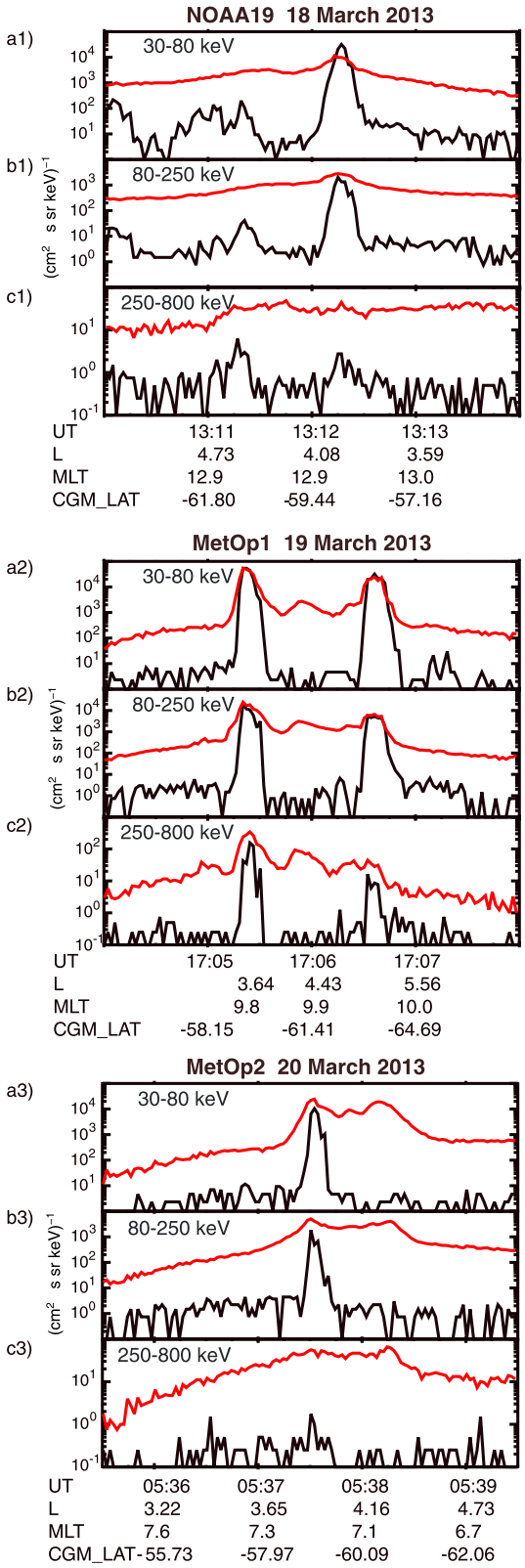

Figure 9. Examples of precipitating (black lines) and trapped (red lines) energetic proton fluxes, at the indicated energies, observed by NOAA and MetOp spacecraft during Case 1 (2013). The three events shown in the top, middle, and bottom sets of panels were selected from Table 1.

6. NOAA/MetOp Observations

For Cases 1 and 2 we carried out a survey of ring current proton precipitation events as measured by the Medium Energy Proton and Electron Detector (MEPED) instrument carried by a set of low-altitude near-polar orbiting POES (NOAA and MetOp) spacecraft. MEPED (Evans & Greer, 2000) measures ion fluxes in three energy bands (30–80 keV, 80–250 keV, and 250–800 keV; Engebretson et al., 2015). From six spacecraft (MetOp 1 and 2 and NOAA 15, 16, 18, and 19) we identified a total of approximately 300 events for the two storm cases. From these, we selected 40 "best" events. The characteristic POES ion precipitation event is described as a latitudinally narrow, strong peak in ion counts in the 0° detector in the 30–80 keV channel. Accumulated experience dating back at least to the work of Lundblad and Soraas (1978) and Søraas et al. (1980, 1999) strongly suggests that such a peaked precipitation flux represents ions that are precipitating as a result of EMIC wave scattering. The "best" events that we selected were the most intense and clearest, including a few of moderate intensity. Of the 300 initially selected POES events, many were less intense and others were either too complex or marginal to be identified with confidence as being related to EMIC waves. A high count rate was regarded as 10,000 $(cm^2\ s\ sr\ keV)^{-1}$ or over and a moderate count rate as 1,000–10,000 $(cm^2\ s\ sr\ keV)^{-1}$. The count rate is a possible proxy for EMIC wave intensity.

A selection of best proton precipitation events for Case 1 is given in Table 1, where we have selected events near $L = 4$ during the storm recovery phase, 18–20 March 2013. This is to coincide with the approximate location and times of the maximum proton spectral intensity as identified from RBSPICE-B and described in section 3. Regarding the notation in Table 1, the proton precipitation flux extends spatially from Min L to Max L and has a maximum intensity at Peak L; amplitude refers to precipitation flux maximum intensity $(cm^2\ s\ sr\ keV)^{-1}$. Similarly in Table 2 we give a selection of best precipitation events for Case 2. Here we choose events near $L = 3$ during the storm recovery period, 18–20 March 2015. The "amplitude" in Tables 1 and 2 was estimated from the time series plots of MEPED data created using the CDAWEB interactive plot facility.

In Figure 9 we illustrate three proton precipitation events selected from Table 1, and in Figure 10, we show three events selected from Table 2. In both figures the black trace (derived from the 0° pitch angle detector) shows the precipitating protons and the red trace (from the 90° detector) shows the trapped protons. Generally, regarding measurements from the POES MEPED instrument, a peak in the 30–80 keV channel is often (but not always) accompanied by a similar weaker peak in the 80–250 keV channel. Peaks in both the 30–80 keV and 80–250 keV channels can be observed in all the events shown in Figures 9 and 10. Further, for each MetOp 1 event in Figure 9, peaks in both the 30–80 keV and 80–250 keV channels are accompanied as well by weaker peaks in the 250–800 keV channel.

EMIC wave-induced proton precipitation events that we identify from POES during the storm recovery periods of Cases 1 and 2 are also indicated by vertical lines in the bottom panels of Figures 11 and 12, respectively; the colors of the vertical lines in the bottom panel

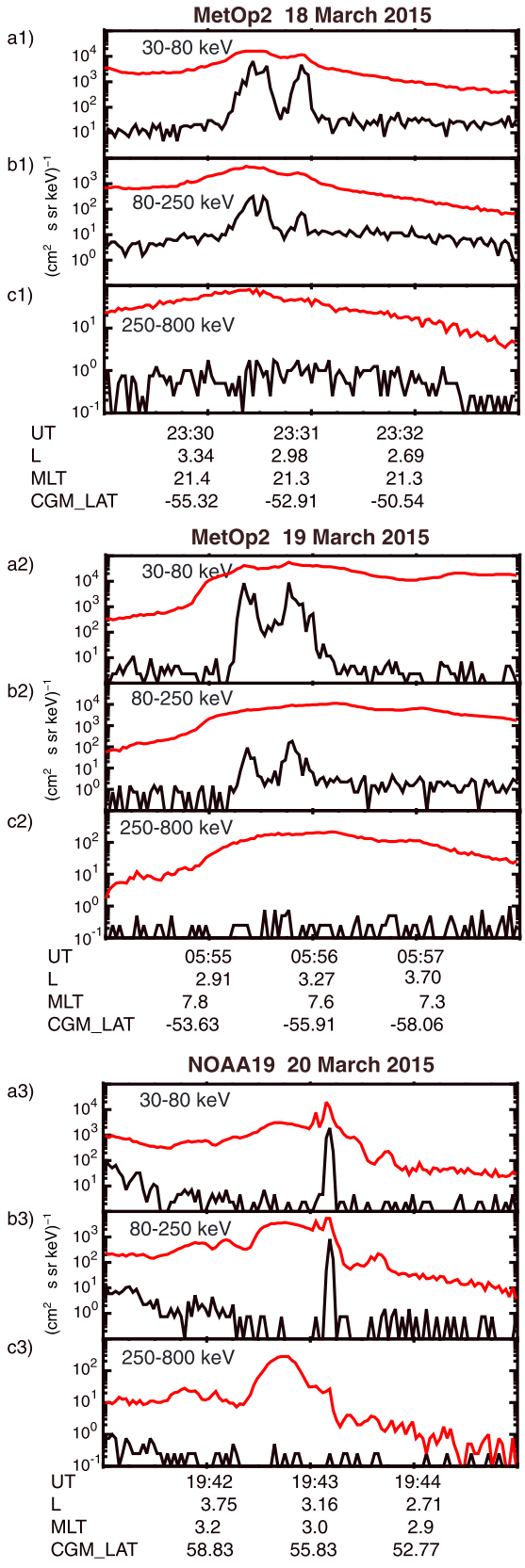

Figure 10. As in Figure 9, except here the three events occurred during Case 2 (2015) and were selected from Table 2.

indicate the approximate *L*-shells at which ring current proton precipitation was observed. Evidently, the POES results we have reported indicate significant EMIC wave activity during the recovery phase of both storms.

We note the recent statistical studies of EMIC waves using Van Allen Probes data by Saikin et al. (2015), Wang et al. (2015), and Zhang et al. (2016). Accordingly, in the following section, we consider only scattering by H^+-band and He^+-band waves and omit consideration of the less frequently occurring O^+-band waves.

7. Comparison of Observed Spectra With Limiting Solutions

In Figure 11 we compare observed proton spectra generated during the Case 1 magnetic storm period against limiting energy spectra. We calculate the limiting spectra by solving the integral equation (4) using a numerical scheme given by Press et al. (2007). We plot the observed spectra at $L \sim 4$, measured during inbound passes in the left panels and outbound passes in the right panels, at selected times during the storm recovery period, 18–20 March 2013. The observed spectra are shown as solid curves, color coded according to UT and orbit number. In the bottom panel of Figure 11, which shows the time profile of the *Dst* index, the colors of the vertical lines indicate the *L*-shells of EMIC wave activity during the recovery period, as deduced from POES observations of ring current proton precipitation. In the top panels of Figure 11 we show the theoretical limiting spectra as dashed curves for the case of a hydrogen plasma ($\eta_1 = 1,\ \eta_2 = 0,\ \eta_3 = 0$) for two different values of the parameter $a = |\Omega_e|^2/\omega_{pe}^2$, namely, $a = 0.01$ and $a = 0.1$. These *a*-values correspond respectively to the approximate background electron number density values $N_0 = 231\ \text{cm}^{-3}$ and $N_0 = 23.1\ \text{cm}^{-3}$, at $L = 4$, assuming a dipole magnetic field. The middle panels of Figure 11 similarly show limiting spectra as dashed curves for the case of a hydrogen-helium plasma ($\eta_1 = 0.75,\ \eta_2 = 0.25,\ \eta_3 = 0$) for the aforementioned values of the parameter *a*. In the top and middle panels we also show the theoretical asymptotic solution given by equation (8) as a solid colored line. In all cases shown in Figure 11 we have set the pitch angle index $s = 0.2$. The value $s = 0.2$ can be considered to be a "generic" value of *s* with respect to the self-limiting flux process; for example, see the discussion by Kennel and Petschek (1966), Mauk and Fox (2010), and Mauk (2013). Regarding the value of the wave gain *G*, which we also require in the solution of equation (4), we set $G = 1.5$, which again is a commonly assumed value in the calculation of self-limiting fluxes, for example, Kennel and Petschek (1966), Schulz and Davidson (1988), and Mauk and Fox (2010).

Within the limits of the uncertainty of the (appropriately averaged) background values of the electron number density N_0, Figure 11 indicates generally that the observed proton spectra are remarkably close to the theoretical limiting spectra. For the case of a hydrogen-helium background plasma, there is relatively close agreement between the observed spectra and the limiting spectra over the energy range from 50 keV to 200 keV. For the case of a hydrogen background plasma, close agreement between the observed and limiting spectra over the range from 50 keV to 200 keV is limited to the lower density ($a = 0.1$)

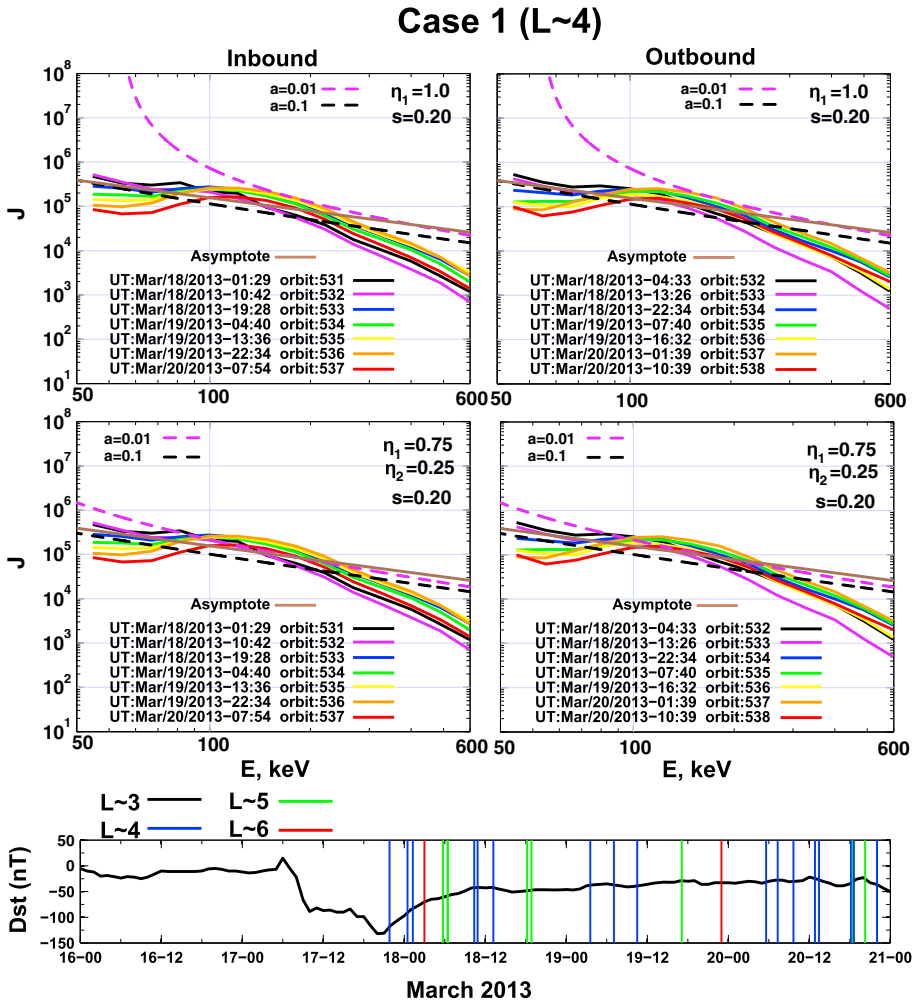

Figure 11. Comparison of RBSPICE-B proton spectra (solid curves) for Case 1 (L ~ 4) with theoretical limiting spectra (dashed curves). The solid colored line in each of the upper four panels represents the theoretical asymptotic solution (8). The vertical colored lines in the bottom panel represent EMIC wave activity as deduced from proton precipitation events observed by MEPED. The colors of the vertical lines indicate the L-shells at which ring current proton precipitation was observed.

case, while for the higher density (a = 0.01) case, such close agreement occurs over the more-limited energy range, 150 keV to 200 keV, approximately.

In Figure 12 we show a comparison of observed energetic proton spectra (solid curves) with theoretical limiting spectra (dashed curves) for the Case 2 storm period. The format of Figure 12 is similar to that of Figure 11, except that for Figure 12, we set L ~ 3 and select observed spectra during the storm recovery period 18–20 March 2015. In this case the chosen a-values, a = 0.01 and a = 0.1 correspond respectively to $N_0 = 1298$ cm^{-3} and $N_0 = 129.8$ cm^{-3} at L = 3 for a dipole field. The colors of the vertical lines in the bottom panel of Figure 12 again indicate times and locations of EMIC wave occurrence during the recovery period, as deduced from POES proton precipitation events. For Case 2 we similarly assume that s = 0.2 and G = 1.5. We also consider the cases of a hydrogen plasma ($\eta_1 = 1$, $\eta_2 = 0$, $\eta_3 = 0$) in the top panels and a hydrogen-helium plasma ($\eta_1 = 0.75$, $\eta_2 = 0.25$, $\eta_3 = 0$) in the middle panels. We see from Figure 12 that agreement between the observed and limiting spectra is quite good over the proton energy range, 100 keV to 300 keV, for the case of a hydrogen-helium plasma. Such reasonable agreement occurs for the case of a hydrogen plasma over the energy range 100 keV to 300 keV only for the lower density (a = 0.1) case. Over the lower energy range, 50 keV to 100 keV, for Case 2, the observed spectra fall somewhat below the theoretical limiting spectra, as shown in each of the top and middle panels of Figure 12.

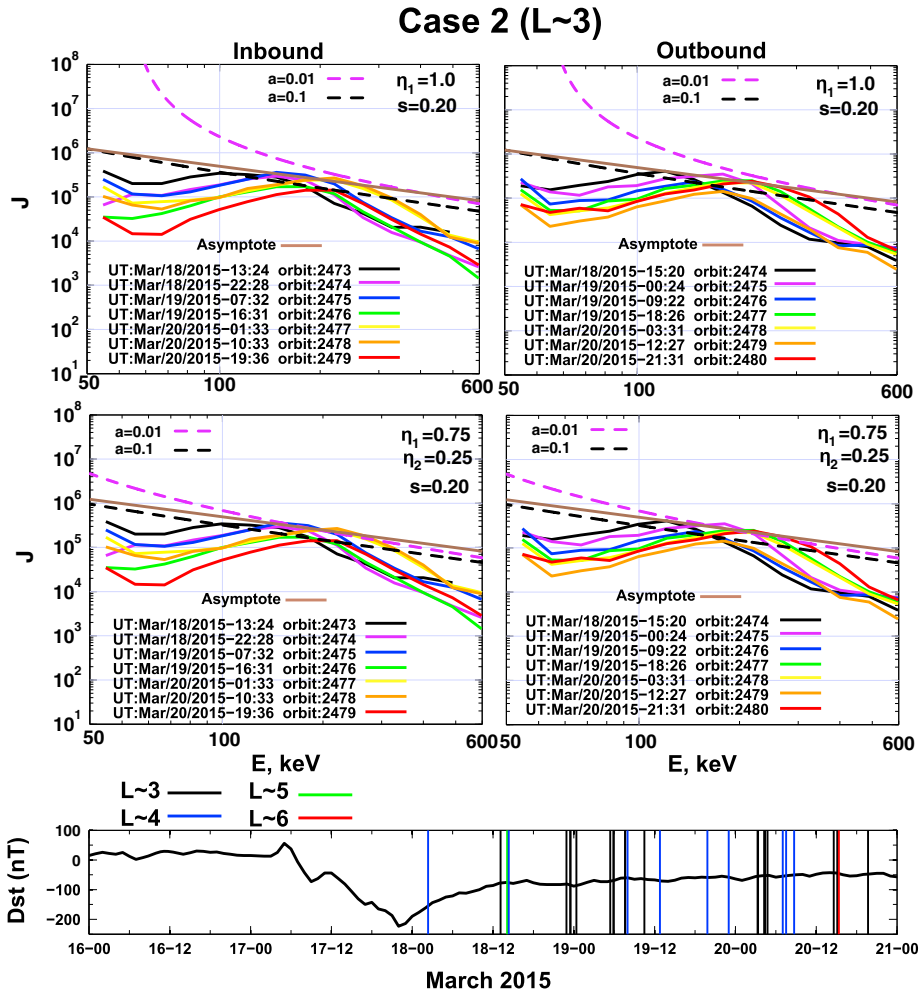

Figure 12. Comparison of RBSPICE-B proton spectra (solid curves) for Case 2 (L ~ 3) with theoretical limiting spectra (dashed curves). The solid colored line in each of the upper four panels represents the theoretical asymptotic solution (8). The vertical colored lines in the bottom panel represent EMIC wave activity as deduced from proton precipitation events observed by MEPED. The colors of the vertical lines indicate the L-shells at which ring current proton precipitation was observed.

The results reported in Figures 11 and 12 provide evidence that proton fluxes are limited by the action of EMIC waves during the recovery periods of both storms over limited energy ranges.

8. Summary and Conclusions

1. We have reported measurements of energetic proton spectra from the RBSPICE-B instrument on the Van Allen Probes, in the region $3 \leq L \leq 6$, during two magnetic storm periods, namely, a strong storm, Case 1, 17–20 March 2013, and a severe storm, Case 2, 17–20 March 2015.
2. Typically, we find that for Case 1, the most intense proton spectra occur at energies, 50 keV–200 keV, in the region $4 \lesssim L < 5$ during the storm recovery period 18–20 March 2013, while for Case 2, the most intense spectra occur for $3 \lesssim L < 4$ at energies 50 keV–300 keV during the recovery period 18–20 March 2015.
3. From a survey of ring current proton precipitation events measured by the MEPED instrument on six POES (NOAA and MetOp) spacecraft, we deduce that EMIC wave activity was significant during the recovery phase of both storms, in particular at L ~ 4 for Case 1 and at L ~ 3 for Case 2.
4. We present a theory that determines the maximum (limiting) ring current proton spectrum resulting from EMIC wave-proton interactions. The limiting spectrum satisfies an integral equation that we solve numerically.

5. For Case 1 at $L \sim 4$, and for Case 2 at $L \sim 3$, we find that the observed most intense proton spectra reasonably match the theoretical (numerically determined) spectra, over prescribed energy ranges. Under these conditions, we therefore deduce that the concept of limitation of ring current proton spectra by EMIC wave scattering can explain the observed intense spectra in the Case 1 and Case 2 storms.

Acknowledgments
This project is supported by a Discovery Grant of the Natural Sciences and Engineering Research Council of Canada to D.S. Proton data used in Figures 2–8 and 11 and 12 are available from RBSPICE via the website http://rbspice.ftecs.com/Data.html. Van Allen Probes orbital information used to construct Figure 1 is likewise available from this website. Profiles of the *Dst* and *Kp* indices were constructed using data from the OMNI website (http://omniweb.gsfc.nasa.gov). The MEPED data plots from the NOAA and MetOp satellites in Figures 9 and 10 were created using the interactive plot facility provided by the Coordinated Data Analysis Web (CDAWeb) at http://cdaweb.sci.gsfc.nasa.gov. We thank David Braun of Augsburg College for assistance in identifying precipitating proton events in the POES data. Work at Augsburg College was supported by U.S. National Science Foundation grants AGS-1264146 and PLR-1341493. K.O. is supported by the Research Council of Norway under contract 223252. K.O. is also grateful for being selected as the 2017–2018 Fulbright Arctic Chair, and his sabbatical at Virginia Tech is sponsored by the U.S. Norway Fulbright Foundation for Educational Exchange.

References

Cornwall, J. M., Coroniti, F. V., & Thorne, R. M. (1970). Turbulent loss of ring current protons. *Journal of Geophysical Research*, *75*, 4699–4709. https://doi.org/10.1029/JA075i025p04699

Cornwall, J. M., Coroniti, F. V., & Thorne, R. M. (1971). Unified theory of SAR arc formation at the plasmapause. *Journal of Geophysical Research*, *76*, 4428–4445. https://doi.org/10.1029/JA076i019p04428

Engebretson, M. J., Posch, J. L., Westerman, A. M., Otto, N. J., Slavin, J. A., Le, G., … Lessard, M. R. (2008). Pc1–Pc2 waves and energetic particle precipitation during and after magnetic storms: Superposed epoch analysis and case studies. *Journal of Geophysical Research*, *113*, A01211. https://doi.org/10.1029/2007JA012362

Engebretson, M. J., Posch, J. L., Wygant, J. R., Kletzing, C. A., Lessard, M. R., Huang, C. L., … Shiokawa, K. (2015). Van Allen probes, NOAA, GOES, and ground observations of an intense EMIC wave event extending over 12 h in magnetic local time. *Journal of Geophysical Research: Space Physics*, *120*, 5465–5488. https://doi.org/10.1002/2015JA021227

Erlandson, R. E., & Ukhorskiy, A. J. (2001). Observations of electromagnetic ion cyclotron waves during geomagnetic storms: Wave occurrence and pitch angle scattering. *Journal of Geophysical Research*, *106*, 3883–3895. https://doi.org/10.1029/2000JA000083

Evans, D. E., & Greer, M. S. (2000). Polar orbiting environmental satellite space environment monitor: 2. Instrument descriptions and archive data documentation, Tech. Rep., Boulder, CO: National Oceanic and Atmospheric Administration.

Finlay, C. C., Maus, S., Beggan, C. D., Hamoudi, M., Lowes, F. J., Olsen, N., & Thébault, E. (2010). Evaluation of candidate geomagnetic field models for IGRF-11. *Earth, Planets and Space*, *62*(10), 787. https://doi.org/10.5047/eps.2010.11.005

Fraser, B. J., Loto'aniu, T. M., & Singer, H. J. (2006). Electromagnetic ion cyclotron waves in the magnetosphere. In K. Takahashi, et al. (Eds.), *Magnetospheric ULF Waves: Synthesis and New Directions Geophys Monogr. Ser* (Vol. 169, pp. 195–212). Washington, DC: American Geophysical Union. https://doi.org/10.1029/169GM13

Jordanova, V. K., Kistler, L. M., Kozyra, J. U., Khazanov, G. V., & Nagy, A. F. (1996). Collisional losses of ring current ions. *Journal of Geophysical Research*, *101*, 111–126. https://doi.org/10.1029/95JA02000

Jordanova, V. K., M. Spasojevic, & M. F. Thomsen (2007). Modeling the electromagnetic ion cyclotron wave-induced formation of detached subauroral proton arcs, *Journal of Geophysical Research*, *112*, A08209. https://doi.org/10.1029/2006JA012215.

Joselyn, J. A., & Lyons, L. R. (1976). Ion cyclotron wave growth calculated from satellite observations of the proton ring current during storm recovery. *Journal of Geophysical Research*, *81*, 2275–2282. https://doi.org/10.1029/JA081i013p02275

Kennel, C. F., & Petschek, H. E. (1966). Limit on stably trapped particle fluxes. *Journal of Geophysical Research*, *71*, 1–28. https://doi.org/10.1029/2009JA014428

Loewe, C. A., & Prölss, G. W. (1997). Classification and mean behavior of magnetic storms. *Journal of Geophysical Research*, *102*, 14,209–14,213. https://doi.org/10.1029/96JA04020

Lundblad, J. A., & Soraas, F. (1978). Proton observations supporting the ion cyclotron wave heating theory of SAR arc formation. *Planetary and Space Science*, *26*(3), 245–254. https://doi.org/10.1016/0032-0633(78)90090-9

Mauk, B. H. (2013). Analysis of EMIC-wave-moderated flux limitation of measured energetic ion spectra in multispecies magnetospheric plasmas. *Geophysical Research Letters*, *40*, 3804–3808. https://doi.org/10.1002/grl.50789

Mauk, B. H. (2014). Comparative investigation of the energetic ion spectra comprising the magnetospheric ring currents of the solar system. *Journal of Geophysical Research: Space Physics*, *119*, 9729–9746. https://doi.org/10.1002/2014JA020392

Mauk, B. H., & Fox, N. J. (2010). Electron radiation belts of the solar system. *Journal of Geophysical Research*, *115*, A12220. https://doi.org/10.1029/2010JA015660

Mauk, B. H., Fox, N. J., Kanekal, S. G., Kessel, R. L., Sibeck, D. G., & Ukhorskiy, A. (2012). Science objectives and rationale for the Radiation Belt Storm Probes mission. *Space Science Reviews*, 1–15. https://doi.org/10.1007/s11214-012-9908-y

Mitchell, D. G., Lanzerotti, L. J., Kim, C. K., Stokes, M., Ho, G., Cooper, S., … Kerem, S. (2013). Radiation Belt Storm Probes Ion Composition Experiment (RBSPICE). *Space Science Reviews*. https://doi.org/10.1007/s11214-013-9965-x

Olson, W. P., & Pfitzer, K. A. (1982). A dynamic model of the magnetospheric magnetic and electric fields for July 29, 1977. *Journal of Geophysical Research*, *87*, 5943–5948. https://doi.org/10.1029/JA087iA08p05943

Press, W. H., Teukolsky, S. A., Vetterling, W. T., & Flannery, B. P. (2007). *Numerical Recipes 3rd Edition: The Art of Scientific Computing*. New York: Cambridge University Press.

Saikin, A. A., Zhang, J.-C., Allen, R. C., Smith, C. W., Kistler, L. M., Spence, H. E., … Jordanova, V. K. (2015). The occurrence and wave properties of H+−, He+−, and O+−band EMIC waves observed by the Van Allen Probes. *Journal of Geophysical Research: Space Physics*, *120*, 7477–7492. https://doi.org/10.1002/2015JA021358

Sakaguchi, K., Shiokawa, K., Miyoshi, Y., Otsuka, Y., Ogawa, T., Asamura, K., & Connors, M. (2008). Simultaneous appearance of isolated auroral arcs and Pc1 geomagnetic pulsations at subauroral latitudes. *Journal of Geophysical Research*, *113*, A05201. https://doi.org/10.1029/2007JA012888

Sandanger, M., Søraas, F., Aarsnes, K., Oksavik, K., & Evans, D. S. (2007). Loss of relativistic electrons: Evidence for pitch angle scattering by electromagnetic ion cyclotron waves excited by unstable ring current protons. *Journal of Geophysical Research*, *112*, A12213. https://doi.org/10.1029/2006JA012138

Schulz, M., & Davidson, G. T. (1988). Limiting energy spectrum of a saturated radiation belt. *Journal of Geophysical Research*, *93*, 59–76. https://doi.org/10.1029/JA093iA01p00059

Søraas, F., Aarsnes, K., Lundblad, J. A., & Evans, D. S. (1999). Enhanced pitch angle scattering of protons at mid-latitudes during geomagnetic storms. *Physics and Chemistry of the Earth, Part C: Solar, Terrestrial & Planetary Science*, *24*(1–3), 287–292. https://doi.org/10.1016/S1464-1917(98)00041-5

Søraas, F., Laundal, K. M., & Usanova, M. (2013). Coincident particle and optical observations of nightside subauroral proton precipitation. *Journal of Geophysical Research: Space Physics*, *118*, 1112–1122. https://doi.org/10.1002/jgra.50172

Søraas, F., Lundblad, J. A., Maltseva, N. F., Troitskaya, V., & Selivanov, V. (1980). A comparison between simultaneous I.P.D.P. groundbased observations and observations of energetic protons obtained by satellites. *Planetary and Space Science*, *28*, 387–405.

Spasojevic, M., Blum, L. W., MacDonald, E. A., Fuselier, S. A., & Golden, D. I. (2011). Correspondence between a plasma-based EMIC wave proxy and subauroral proton precipitation. *Geophysical Research Letters*, *38*, L23102. https://doi.org/10.1029/2011GL049735

Summers, D. (2005). Quasi-linear diffusion coefficients for field-aligned electromagnetic waves with applications to the magnetosphere. *Journal of Geophysical Research*, *110*, A08213. https://doi.org/10.1029/2005JA011159

Summers, D., & Shi, R. (2014). Limiting energy spectrum of an electron radiation belt. *Journal of Geophysical Research: Space Physics*, *119*, 6313–6326. https://doi.org/10.1002/2014JA020250

Summers, D., & Shi, R. (2015). Limitation of energetic ring current ion spectra. *Journal of Geophysical Research: Space Physics*, *120*, 7374–7389. https://doi.org/10.1002/2015JA021482

Summers, D., Tang, R., & Omura, Y. (2011). Effects of nonlinear wave growth on extreme radiation belt electron fluxes. *Journal of Geophysical Research*, *116*, A10226. https://doi.org/10.1029/2011JA016602

Summers, D., Tang, R., & Thorne, R. M. (2009). Limit on stably trapped particle fluxes in planetary magnetospheres. *Journal of Geophysical Research*, *114*, A10210. https://doi.org/10.1029/2009JA014428

Tang, R., & Summers, D. (2012). Energetic electron fluxes at Saturn from Cassini observations. *Journal of Geophysical Research*, *117*, A06221. https://doi.org/10.1029/2011JA017394

Usanova, M. E., Mann, I. R., Kale, Z. C., Rae, I. J., Sydora, R. D., Sandanger, M., … Vallières, X. (2010). Conjugate ground and multisatellite observations of compression-related EMIC Pc1 waves and associated proton precipitation. *Journal of Geophysical Research*, *115*, A07208. https://doi.org/10.1029/2009JA014935

Wang, D., Yuan, Z., Yu, X., Deng, X., Zhou, M., Huang, S., … Wygant, J. R. (2015). Statistical characteristics of EMIC waves: Van Allen Probe observations. *Journal of Geophysical Research: Space Physics*, *120*, 4400–4408. https://doi.org/10.1002/2015JA021089

Xiao, F., C. Yang, Q. Zhou, Z. He, Y. He, X. Zhou, & L. Tang (2012). Nonstorm time scattering of ring current protons by electromagnetic ion cyclotron waves. *Journal of Geophysical Research*, *117*, A08204. https://doi.org/10.1029/2012JA017922

Xiong, Y., Yuan, Z., & Wang, J. (2016). Energetic ions scattered into the loss cone with observations of the Cluster satellite. *Annales de Geophysique*, *34*, 249–257. https://doi.org/10.5194/angeo-34-249-2016

Yahnin, A. G., & Yahnina, T. A. (2007). Energetic proton precipitation related to ion-cyclotron waves. *Journal of Atmospheric and Solar: Terrestrial Physics*, *69*, 1690–1706. https://doi.org/10.1016/j.jastp.2007.02.010

Yahnina, T. A., Yahnin, A. G., Kangas, J., & Manninen, J. (2000). Proton precipitation related to Pc1 pulsations. *Geophysical Research Letters*, *27*, 3575–3578. https://doi.org/10.1029/2000GL003763

Yahnina, T. A., Yahnin, A. G., Kangas, J., & Manninen, J. (2002). Localized enhancements of energetic proton fluxes at low altitudes in the subauroral region and their relation to Pc1 pulsations. *Cosmic Research*, *40*, 213–223. https://doi.org/10.1023/A:1015968702640

Yahnina, T. A., Yahnin, A. G., Kangas, J., Manninen, J., Evans, D. S., Demekhov, A. G., … Gvozdevsky, B. B. (2003). Energetic particle counterparts for geomagnetic pulsations of Pc1 and IPDP types. *Annales de Geophysique*, *21*, 2281–2292.

Yuan, Z., Xiong, Y., Li, H., Huang, S., Qiao, Z., Wang, Z., … Wang, J. (2014). Influence of precipitating energetic ions caused by EMIC waves on the subauroral ionospheric E region during a geomagnetic storm. *Journal of Geophysical Research: Space Physics*, *119*, 8462–8471. https://doi.org/10.1002/2014JA020303

Yuan, Z., Xiong, Y., Qiao, Z., Li, H., Huang, S., Wang, D., … Wang, J. (2016). A subauroral polarization stream driven by field-aligned currents associated with precipitating energetic ions caused by EMIC waves: A case study. *Journal of Geophysical Research: Space Physics*, *121*, 1696–1705. https://doi.org/10.1002/2015JA021804

Zhang, X.-J., Li, W., Thorne, R. M., Angelopoulos, V., Bortnik, J., Kletzing, C. A., … Hospodarsky, G. B. (2016). Statistical distribution of EMIC wave spectra: Observations from Van Allen Probes. *Geophysical Research Letters*, *43*, 12,348–12,355. https://doi.org/10.1002/2016GL071158

Erratum

In the originally published version of this article, an error was introduced at the beginning of section 3 that caused the term "Case 1" to be repeated erroneously before the dates 17-20 March 2015 in place of the correct "Case 2". This error has been corrected, and the present version may be considered the authoritative version of record.